Staining algorithm for seismic modeling and migration

Bo Chen[1] and Xiaofeng Jia[1]

ABSTRACT

In seismic migration, some structures such as those in subsalt shadow zones are not imaged well. The signal in these areas may be even weaker than the artifacts elsewhere. We evaluated a method to significantly improve the signal-to-noise ratio (S/N) in poorly illuminated areas of the model. We constructed a "phantom" wavefield: an extension of the wavefield to the complex domain. The imaginary wavefield was synchronized with the real wavefield, but it contained only the events relevant to a target region of the model, which was specified using a staining algorithm. The real wavefield interacted with the entire model. However, all structures except for the target were transparent to the imaginary wavefield, which is excited only when the real wavefront arrives at the target structure. The real and the imaginary source wavefields were crosscorrelated with the regular receiver wavefield. The results were revealed in two images: the conventional reverse time migration image and an image of the target region only. Synthetic experiments showed that the S/N of the target structures was improved significantly, with other structures effectively muted.

INTRODUCTION

Seismic migration is one of the most important processing techniques that focuses reflections and diffractions and yields seismic images of subsurface areas. Generally, those images are often used in further processing and interpretation. However, when dealing with critical areas such as overhanging structures and subsalt shadow zones, seismic migration may generate poorly focused images. This defect is usually caused by three factors: improper choice of migration methods, inaccurate estimation of the velocity model, and inadequate data acquisition. Currently, there are three kinds of migration methods commonly used in practice: ray- or beam-based migration, one-way wave-equation-based migration, and full-wave-equation-based migration. Ray-based migration (Albertin et al., 2002; Fowler et al., 2004) can image steep structures effectively; however, it produces relatively low signal-to-noise ratio (S/N) images for subsalt regions. The one-way wave propagator fails to simulate wide-angle and turning waves, which are useful for imaging steep and overhanging structures (Ristow and Ruhl, 1994; Mulder and Plessix, 2004). Zhang and McMechan (1997) use a horizontal extrapolation scheme to overcome the angle limitation of conventional one-way propagators. Tilted coordinates (Sava and Fomel, 2005; Shragge and Shan, 2008) can be used to fit the target reflector dip. Jia and Wu (2009) develop a super-wide-angle wavefront reconstruction method to handle the wide-angle problem and provide good images of steep features and overhanging salt flanks. Based on the two-way wave equation, reverse time migration (RTM) (Baysal et al., 1983; McMechan, 1983; Mulder and Plessix, 2004) has excellent performance in steep dip and subsalt imaging in spite of its relatively low efficiency.

Apart from the propagator, the poor images of some critical structures, especially in subsalt regions, are caused by inadequate acquisition of seismic signals. Imaging the subsalt area is a challenging problem because seismic wavefields are strongly distorted when propagating through the high-velocity salt bodies. The salt body can significantly block the energy, creating uneven illumination and shadow zones (Jackson et al., 1994; Muerdter and Ratcliff, 2001; Leveille et al., 2011; Liu et al., 2011). In such critical subsalt areas, valuable signals are diminished further and are weaker than the artifacts elsewhere. Several approaches have been proposed for improving the images of subsalt areas. Illumination compensation for subsalt imaging (Gherasim et al., 2010; Shen et al., 2011; Yang et al., 2012) can enhance the signals of poorly illuminated subsalt areas. Acquisition aperture correction (Cao and Wu, 2009) can improve the image amplitude greatly. Malcolm et al. (2008) use multiple scattered waves to image subsalt structures that are not easily illuminated by primaries. Liu et al. (2011) modify conventional RTM and use the multiples as constructive energy for imaging. Velocity model build-

ing plays an important role to enhance the subsalt visibility and resolution (Fliedner et al., 2007; Wang et al., 2008; Ji et al., 2011). A target-oriented strategy using a data set obtained by generalized Born modeling based on a single scattering approximation to the full wave equation can use wavefield-based velocity estimation to focus on improving velocities in subsalt regions (Tang and Biondi, 2011). In addition, others focus effort on investigating the impact of acquisition geometries on subsalt imaging (Kapoor et al., 2007; VerWest and Lin, 2007; Burch et al., 2010; Zhu et al., 2012).

In developmental biology, a method called *fate mapping* (Dale and Slack, 1987; Gilbert, 2000; Ginhoux et al., 2010) establishes the correspondence between individual cells (or groups of cells) at one stage of development and their progeny at later stages of development. This technique is used for understanding the embryonic origin of various tissues in the adult organism. Embryologists use "vital dyes" (which would stain but not harm the cells) to follow movements of individual cells or groups of cells over time in embryos. The tissues to which the cells contribute would thus be labeled and visible in the adult organism. In this paper, we use the concept of fate mapping and implement it in wave propagation. We establish the correspondence between the wavefield and certain desired critical subsurface structures, and we take advantage of the correspondence to obtain high-quality images of the target structures without the influence of other unconcerned structures. Though not being able to produce true amplitudes currently, this method is a heuristic approach to manipulate the wavefield and the imaging process in a useful way.

STAINING ALGORITHM

We propose an algorithm that can trace the wavefront passing a target structure and identify the origin of a particular reflection. If the wavefront reaches nontarget structures, no response tends to occur as if the medium was transparent; however, once the wavefront touches the target structure, reflection and transmission occur normally and will be labeled and traced in subsequent propagation. The wavefront that has touched the target structure can be discriminated during propagation, and reflections from the target structure can be identified and separated in the wavefield or the seismic data. Because this mechanism is like identifying and tracing a single person who has touched wet paint on a wall from a group of people, we name the method a *staining algorithm*. In fate mapping, this staining is implemented using dye to stain the cells, which labels and traces them in subsequent development; however, in seismology, our "dye" is a spatial function that labels the target structure and traces the wavefront passing the labeled structure.

Wave equation in the complex domain

The equation used in this research is the constant-density 2D full acoustic wave equation given by

$$\frac{\partial^2 p}{\partial t^2} = v^2 \Delta p, \tag{1}$$

where $\Delta = (\partial^2/\partial x^2 + \partial^2/\partial z^2)$ is the Laplace operator, $p = p(x, z, t)$ is the pressure wavefield at a spatial location (x, z) and time t, and $v = v(x, z)$ is the velocity. To construct a "phantom" wavefield that is synchronized with the real one but only contains the reflections and transmissions relevant to the target structure, we extend all the variables to the complex domain; i.e.,

$$p = p(x, z, t) = \bar{p} + i\tilde{p}, \tag{2}$$

$$v = v(x, z) = \bar{v} + i\tilde{v}, \tag{3}$$

where $i = \sqrt{-1}$, the overbar $-$ in all variables denotes the real part, and the tilde $\tilde{}$ denotes the imaginary part. Substituting equations 2 and 3 into equation 1, we have the wave equation in the complex domain expressed as

$$\frac{\partial^2(\bar{p} + i\tilde{p})}{\partial t^2} = (\bar{v} + i\tilde{v})^2(\Delta\bar{p} + i\Delta\tilde{p}). \tag{4}$$

Expanding equation 4, we have

$$\frac{\partial^2(\bar{p} + i\tilde{p})}{\partial t^2} = (\bar{v}^2 - \tilde{v}^2)\Delta\bar{p} - 2\bar{v}\,\tilde{v}\,\Delta\tilde{p} + i(\bar{v}^2 - \tilde{v}^2)\Delta\tilde{p}$$
$$- 2i\bar{v}\,\tilde{v}\,\Delta\bar{p}. \tag{5}$$

If $\tilde{v} \to 0$, all terms containing $\tilde{v}$ can be ignored; thus, equation 5 is simplified as

$$\frac{\partial^2(\bar{p} + i\tilde{p})}{\partial t^2} = \bar{v}^2\Delta\bar{p} + i\bar{v}^2\Delta\tilde{p} = \bar{v}^2\Delta(\bar{p} + i\tilde{p}). \tag{6}$$

Rewriting equation 6 by separating the real and the imaginary parts, we have

$$\frac{\partial^2\bar{p}}{\partial t^2} = \bar{v}^2\Delta\bar{p}, \tag{7}$$

$$\frac{\partial^2\tilde{p}}{\partial t^2} = \bar{v}^2\Delta\tilde{p}. \tag{8}$$

We call $\bar{p}$ the *real wavefield* and $\tilde{p}$ the *imaginary wavefield*. Comparing equations 7 and 8 with equation 1, we find that $\bar{p}$ and $\tilde{p}$ follow the same wave equation, which indicates that the imaginary wavefield is synchronized with the real wavefield in the propagation.

Excitement and synchronization of the imaginary wavefield

We use the finite-difference (FD) method to solve the wave equation. Denote

$$p^l_{m,n} = p(mh, nh, l\tau), \tag{9}$$

$$v_{m,n} = v(mh, nh), \tag{10}$$

where τ is the time step, h is the grid interval, m and n are the spatial indices, and l is the temporal index. We discuss the second-order temporal and spatial accuracy FD scheme for simplicity. The temporal derivative is expressed as

$$\left.\frac{\partial^2 p}{\partial t^2}\right|_{x,z,t} \approx \frac{1}{\tau^2}(p^{l+1}_{m,n} - 2p^l_{m,n} + p^{l-1}_{m,n}), \tag{11}$$

and the spatial derivatives are expressed as

$$\left.\frac{\partial^2 p}{\partial x^2}\right|_{x,z,t} \approx \frac{1}{h^2}(p_{m+1,n}^l - 2p_{m,n}^l + p_{m-1,n}^l), \qquad (12)$$

$$\left.\frac{\partial^2 p}{\partial z^2}\right|_{x,z,t} \approx \frac{1}{h^2}(p_{m,n+1}^l - 2p_{m,n}^l + p_{m,n-1}^l). \qquad (13)$$

Substituting equations 11–13 into equation 1, we have the wave equation discretized as

$$p_{m,n}^{l+1} - 2p_{m,n}^l + p_{m,n}^{l-1}$$
$$= v^2\lambda^2(p_{m+1,n}^l + p_{m-1,n}^l + p_{m,n+1}^l + p_{m,n-1}^l - 4p_{m,n}^l), \qquad (14)$$

where $\lambda = \tau/h$.

Hence, the explicit FD iteration scheme is expressed as

$$p_{m,n}^{l+1} = v^2\lambda^2(p_{m+1,n}^l + p_{m-1,n}^l + p_{m,n+1}^l + p_{m,n-1}^l - 4p_{m,n}^l)$$
$$+ 2p_{m,n}^l - p_{m,n}^{l-1}. \qquad (15)$$

Denoting

$$P^l = \lambda^2(p_{m+1,n}^l + p_{m-1,n}^l + p_{m,n+1}^l + p_{m,n-1}^l - 4p_{m,n}^l), \qquad (16)$$

the iteration scheme can be simplified as

$$p_{m,n}^{l+1} = v^2 P^l + 2p_{m,n}^l - p_{m,n}^{l-1}. \qquad (17)$$

To implement the staining algorithm, we extend all the variables to the complex domain; i.e.,

$$p_{m,n}^l = \bar{p}_{m,n}^l + i\tilde{p}_{m,n}^l, \qquad (18)$$

$$P^l = \bar{P}^l + i\tilde{P}^l, \qquad (19)$$

$$v_{m,n} = \bar{v}_{m,n} + i\tilde{v}_{m,n}. \qquad (20)$$

Substituting equations 18–20 into equation 17, we have the iteration scheme in the complex domain expressed as

$$(\bar{p}_{m,n}^{l+1} + i\tilde{p}_{m,n}^{l+1}) = (\bar{v}_{m,n} + i\tilde{v}_{m,n})^2(\bar{P}^l + i\tilde{P}^l)$$
$$+ 2(\bar{p}_{m,n}^l + i\tilde{p}_{m,n}^l) - (\bar{p}_{m,n}^{l-1} + i\tilde{p}_{m,n}^{l-1}). \qquad (21)$$

According to equation 21, the iteration schemes in the real and the imaginary domains are expressed as follows:

$$\bar{p}_{m,n}^{l+1} = \bar{v}_{m,n}^2\bar{P}^l + 2\bar{p}_{m,n}^l - \bar{p}_{m,n}^{l-1} - 2\bar{v}_{m,n}\tilde{v}_{m,n}\tilde{P}^l - \tilde{v}_{m,n}^2\bar{P}^l, \qquad (22)$$

$$\tilde{p}_{m,n}^{l+1} = \bar{v}_{m,n}^2\tilde{P}^l + 2\tilde{p}_{m,n}^l - \tilde{p}_{m,n}^{l-1} + 2\bar{v}_{m,n}\tilde{v}_{m,n}\bar{P}^l - \tilde{v}_{m,n}^2\tilde{P}^l. \qquad (23)$$

For the real-domain FD iteration (equation 22), in the computation of the real wavefield, the source is injected by adding the discretized wavelet directly to the wavefield; i.e.,

$$\bar{p}_{m,n}^{l+1} = \bar{v}_{m,n}^2\bar{P}^l + 2\bar{p}_{m,n}^l - \bar{p}_{m,n}^{l-1} - 2\bar{v}_{m,n}\tilde{v}_{m,n}\tilde{P}^l$$
$$- \tilde{v}_{m,n}^2\bar{P}^l + s_{re}^{l+1}, \qquad (24)$$

where s_{re}^{l+1} is the discretized source wavelet. As mentioned above, theoretically, all terms containing $\tilde{v}_{m,n}$ can be ignored if $\tilde{v}_{m,n} \to 0$. To quantitatively analyze the influence of $\tilde{v}_{m,n}$, we define

$$\gamma(k) = \frac{\max|p(x,z) - \bar{p}^{(k)}(x,z)|}{\max|p(x,z)|}, \qquad (25)$$

where $p(x,z)$ is the wavefield calculated in the conventional way using the wave equation in the real domain and $\bar{p}^{(k)}(x,z)$ is calculated by equation 24 with $\tilde{v}_{m,n}$ k orders of magnitude smaller than $\bar{v}_{m,n}$. The term $\gamma(k)$ is a key factor to determine the order of magnitude of $\tilde{v}_{m,n}$ in the computation. The staining mechanism is implemented by assigning an infinitesimal value to the imaginary part of the velocity; i.e.,

$$\bar{v}_{m,n} = v_{m,n}, \tilde{v}_{m,n}\begin{cases} \neq 0, & \text{target structure} \\ = 0, & \text{otherwise} \end{cases}. \qquad (26)$$

Practically, when $\tilde{v}_{m,n}$ is of the 10^{-6} order of magnitude, $\gamma(k)$ is zero with the computer program using single-precision real-type variables. In this case, we can ignore the terms of $\tilde{v}_{m,n}$ in equation 24 and obtain the real-domain iteration scheme:

$$\bar{p}_{m,n}^{l+1} = \bar{v}_{m,n}^2\bar{P}^l + 2\bar{p}_{m,n}^l - \bar{p}_{m,n}^{l-1} + s_{re}^{l+1}. \qquad (27)$$

For the imaginary-domain FD iteration equation 23, we can first ignore the second-order term $\tilde{v}_{m,n}^2\bar{P}^l$. Equation 23 can be written as

$$\tilde{p}_{m,n}^{l+1} = \bar{v}_{m,n}^2\tilde{P}^l + 2\tilde{p}_{m,n}^l - \tilde{p}_{m,n}^{l-1} + 2\bar{v}_{m,n}\tilde{v}_{m,n}\bar{P}^l. \qquad (28)$$

We now discuss the property of the term $2\bar{v}_{m,n}\tilde{v}_{m,n}\bar{P}^l$ and how $\tilde{p}_{m,n}$ is excited. For any point except for the source location, $\bar{p}_{m,n}^0 = \bar{p}_{m,n}^{-1} = 0$ and $\tilde{p}_{m,n}^0 = \tilde{p}_{m,n}^{-1} = 0$. Suppose only one single point (m_0, n_0) is stained, i.e., $\tilde{v}_{m_0,n_0} \neq 0$, and the first arrival in the real domain comes at the time step l_0; i.e., $\bar{p}_{m_0,n_0}^l = 0$ when $l < l_0$. According to equation 28, if and only if $\tilde{v}_{m,n} \neq 0$ and $\bar{P}^l \neq 0$, i.e., $2\bar{v}_{m,n}\tilde{v}_{m,n}\bar{P}^l \neq 0$, the imaginary wavefield can be excited. That is, the imaginary wavefield is generated once the real wavefield hits the stained target. When the wavefront in the real domain has passed the stained point (m_0, n_0), $\bar{P}^l$ becomes zero, leading to $2\bar{v}_{m,n}\tilde{v}_{m,n}\bar{P}^l = 0$. Consequently, the term $2\bar{v}_{m,n}\tilde{v}_{m,n}\bar{P}^l$ can be regarded as a source term injected automatically by the staining algorithm. We have equation 28 rewritten as

$$\tilde{p}_{m,n}^{l+1} = \bar{v}_{m,n}^2\tilde{P}^l + 2\tilde{p}_{m,n}^l - \tilde{p}_{m,n}^{l-1} + s_{im}^{l+1}, \qquad (29)$$

where $s_{m,n}^{l+1} = 2\bar{v}_{m,n}\tilde{v}_{m,n}\bar{P}^l$.

Comparing equation 27 with equation 29, we find that $\bar{p}_{m,n}$ and $\tilde{p}_{m,n}$ have the same iteration scheme, which indicates that the imaginary wavefield is synchronized with the real wavefield and excited at the stained structure. In the real domain, the wavefront propagates normally without interference. Meanwhile, in the imaginary domain, only when the wavefront in the real domain arrives at the stained target structure (where $\tilde{v}_{m,n} \neq 0$) are the stained points triggered as point sources. According to Huygens' principle (Sheriff and Geldart, 1995), every point on a wavefront can be regarded

as a new source of waves. Thus, the imaginary wavefield is excited by these point sources and synchronized with the real wavefield in the subsequent propagation as demonstrated in equations 27 and 29. The selectively excited imaginary wavefield can provide phase information mapping to the real wavefield; thus, all responses related to the target structure are "stained" and can be traced and identified. We call the surface data obtained in the real domain $D_{re}(x, z = 0, t)$ *real data*, and the data obtained in the imaginary domain $D_{im}(x, z = 0, t)$ *imaginary data*. According to the excitement of the imaginary wavefield, imaginary data are synchronized with and are part of the real data.

Imaging condition

The staining algorithm can be applied to seismic migration to obtain an image of the target structure. The migration method used in this study is RTM, which consists of three main steps (Symes, 2007): (1) extrapolate the forward-propagating shot wavefield $S(x, z, t)$, (2) extrapolate the backward-propagating receiver wavefield $G(x, z, t)$, and (3) apply the imaging condition to obtain the image. We can apply the staining algorithm by modifying steps 1 and 3. The receiver wavefield is computed conventionally in the real domain with recorded data as virtual sources. However, the shot wavefield is computed in the complex domain with the stained complex velocity model, and the real shot wavefield $S_{re}(x, z, t)$ and the imaginary shot wavefield $S_{im}(x, z, t)$ are obtained together. Subsequently, the two shot wavefields are crosscorrelated with the conventional receiver wavefield, respectively. Imaging conditions can be expressed as

$$I_{re}(x, z) = \int_0^T S_{re}(x, z, t) G(x, z, T - t) \mathrm{d}t, \qquad (30)$$

$$I_{im}(x, z) = \int_0^T S_{im}(x, z, t) G(x, z, T - t) \mathrm{d}t, \qquad (31)$$

where $G(x, z, t)$ is the receiver wavefield. The term $I_{re}(x, z)$ is the *real image* that is exactly the same as the result of conventional RTM, and $I_{im}(x, z)$ is the *imaginary image* that can be considered as the image of the target region.

NUMERICAL EXAMPLES

We have conducted numerical experiments on a series of velocity models to show the application of the staining algorithm to seismic modeling and migration. The propagator used in the experiment is an eighth-order spatial and second-order temporal accuracy explicit FD scheme.

Figure 1 shows the excitement and synchronization of the imaginary wavefield. Figure 1a shows a simple model in the complex domain with the velocities of each layer 2.5, 3.5, and 4.5 km/s, respectively, in the real part, and the reflector at depth 4.4 km stained by assigning 1.0×10^{-6} to the imaginary part. The shot is located at 4 km on the surface, and geophones are distributed from 0 to 4 km with an interval of 8 m. When the wavefront in the real domain arrives at the nonstained reflector at 2.4 km, reflection and transmission occur in the real wavefield normally; however, in the imaginary wavefield, no responses occur because no stained structure has been touched yet. When the wavefront in the real domain arrives at the stained reflector at 4.4 km, the points

on the interface are successively activated and excite the imaginary wavefield as point sources. Figure 1b and 1d shows snapshots of the real wavefield at 1.8 and 2.2 s, respectively; Figure 1c and 1e shows the corresponding snapshots of the imaginary wavefield. Comparing the snapshots of the real and the imaginary wavefield, we find that the imaginary wavefield is synchronized with the real wavefield in propagation after being excited. Because the imaginary wavefield is not excited before the wavefront in the real domain arrives at the stained interface, it only contains the reflection and transmission relevant to the stained reflector excluding the ones relevant to other nonstained structures. Figure 2 shows the seismograms of the real and the imaginary wavefields recorded at the point (4 km, 2.4 km). The response at 1.032 s in the real domain is the direct arrival to the reflector at 2.4 km, and the response at 2.175 s is the reflection from the stained reflector at 4.4 km. The imaginary wavefield is not excited until the wavefront arrives at the stained reflector at 1.603 s. Consequently, the directly arrival does not appear in the imaginary domain and only the reflection from the stained reflector is recorded. The reflection in the imaginary domain is synchronized with that in the real domain.

Figure 3 shows the difference of the wavefield calculated in the conventional real domain and the corresponding real wavefield calculated in the complex domain, i.e., $p(x, z) - \bar{p}^{(k)}(x, z)$. The imaginary velocity $\tilde{v}_{m,n}$ used for the calculation ranges from 2 to 5 orders of magnitude smaller than the real velocity $\bar{v}_{m,n}$. The difference illustrated in the figure is the ignored term in equation 22. When the order of magnitude reduces to 10^{-6} (i.e., $k = 6$), the difference becomes zero in the computation using single-precision real-type variables, which indicates that the real wavefield calculated by staining algorithm is not affected by the imaginary one and is identical to the one calculated in the conventional way. Table 1 shows the magnitude of the maximal difference and $\gamma(k)$ with the variation of k corresponding to Figure 1b.

Figure 4a and 4b shows the real surface data and the imaginary data of Figure 1a, respectively. In the imaginary data, the direct wave and responses from the reflector at 2.4 km are absent as if the medium above the stained interface was transparent. Figure 4c and 4d is obtained using the real and imaginary data above, respectively, for conventional real-domain RTM. Compared with Figure 4c, the reflector at 2.4 km is not imaged in Figure 4d, which proves that the imaginary data only contain the reflections relevant to the stained interface.

The results of a complex velocity model are shown in Figure 5. Figure 5a is the Sigsbee2A model, in which the sediment between the two white arrows is the stained target structure. Figure 5b and 5c shows the real and imaginary data, respectively. The shot is located at 13.26 km, and the geophones are distributed from 0 to 24.39 km with an interval of 11.43 m. Figure 5d and 5e is obtained using the data shown in Figure 5b and 5c, respectively, for conventional real-domain RTM. From the tests above, we can see the imaginary wavefield and the imaginary data obtained by staining algorithm only contain the responses relevant to the stained target structure.

Figures 6 and 7 show the application of the staining algorithm to migration. In these tests, all the data used for the computation are conventional recorded data, not the imaginary data we generated by the staining algorithm and those used in the previous tests. The real image and the imaginary image are obtained from the same data set, and by imaging condition equations 30 and 31, respectively. Some critical structures are selected to verify the validity of the staining

algorithm in migration. The results of the numerical test on the SEG/EAGE model are shown in Figure 6. The target subsalt structure is marked in the model shown in Figure 6a. The real image (the same as the one by conventional RTM) and the imaginary image

(image of the target structure) are obtained simultaneously, and they are shown in Figure 6b and 6c, respectively. Due to weak illumination and the masking of the salt above, the structure under the salt is not well imaged by conventional RTM. By using the staining
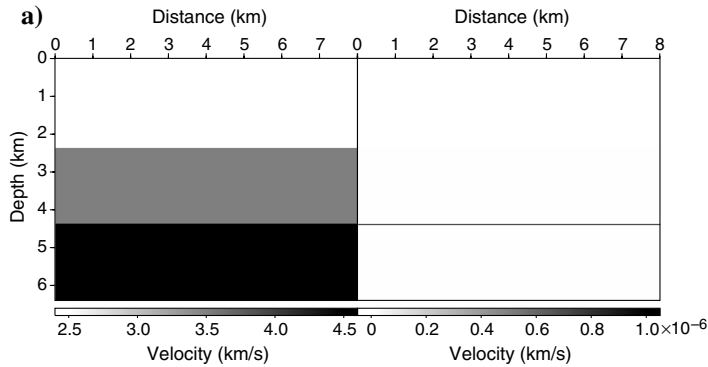
Figure 1. (a) Stained velocity model in the complex domain. The left is the real part with velocities of each layer 2.5, 3.25, and 4.5 km/s, respectively. The right is the imaginary part with the points on the reflector at 4.4 km 1.0×10^{-6} and elsewhere zero. (b) Snapshot of the real wavefield at 1.8 s. (c) Snapshot of the imaginary wavefield corresponding to (b). (d) Snapshot of the real wavefield at 2.2 s. (e) Snapshot of the imaginary wavefield corresponding to (d).
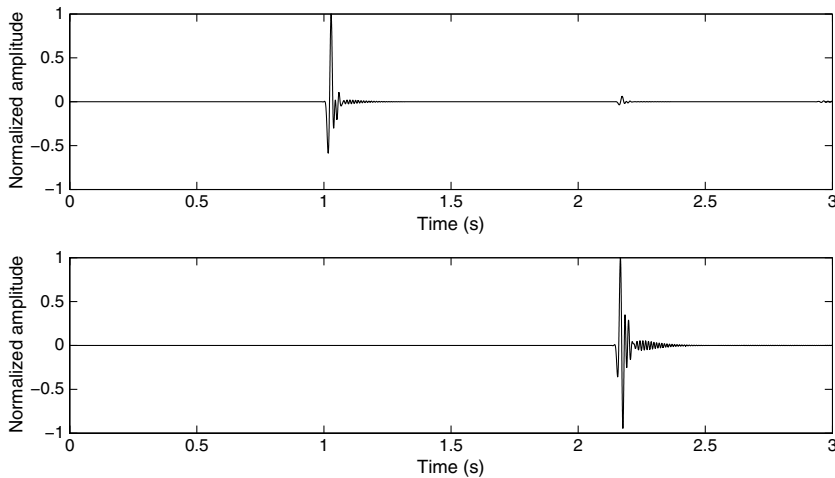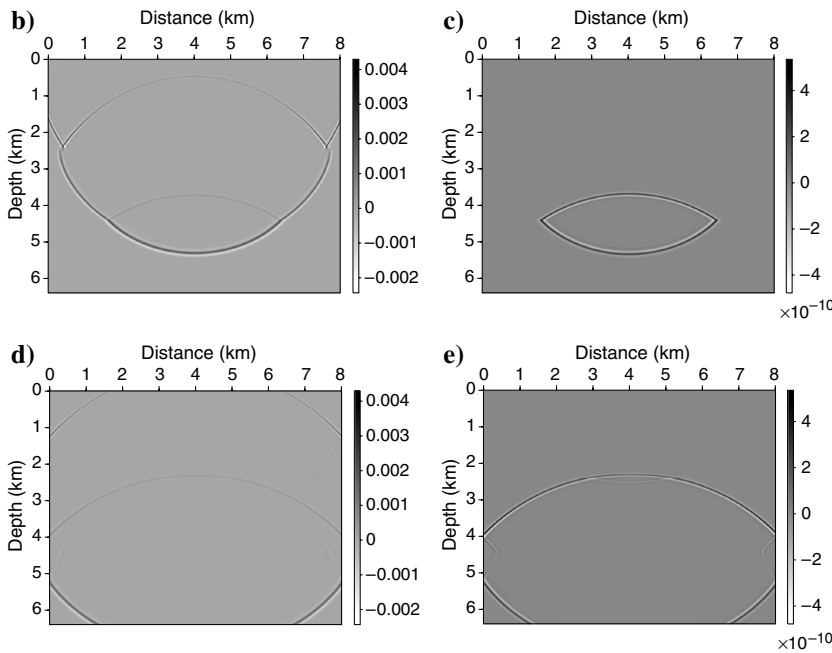
Figure 2. Seismogram in the real (the top) and the imaginary (the bottom) domains recorded at (4 km, 2.4 km). The record length is 3 s, and the amplitude of each is normalized to 1. The source is a Ricker wavelet with dominant frequency of 40 Hz and time shift of 0.072 s.

algorithm, the salt is effectively muted in the image, and the target structure is specifically and clearly imaged. The BP salt dome model and relevant results are shown in Figure 7. Figure 7a is

the velocity model with the overhanging structure (the white dashed line) and part of the inner boundary of the salt (the white solid line) marked as the target structures. Compared with the real image

Figure 3. The difference (as a function of k) between the wavefield calculated in the real domain $p(x, z)$ (the one shown in Figure 1b) and the real wavefield calculated in the complex domain $\bar{p}^{(k)}(x, z)$.
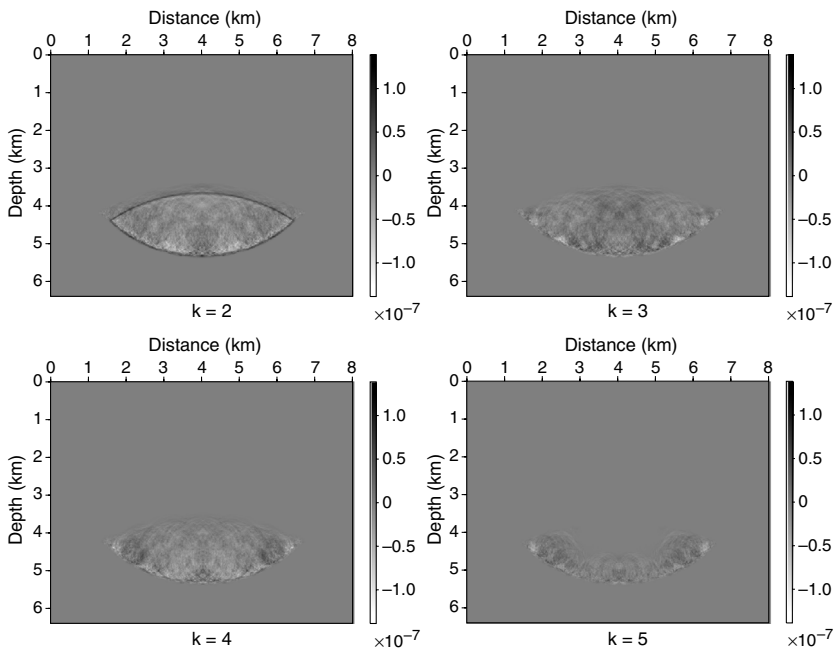
Figure 4. (a) Real surface data of Figure 1a. The shot is located at 4 km, and the geophones are distributed from 0 to 4 km with an interval of 8 m. (b) Imaginary data corresponding to (a). (c) Imaging result of (a) by conventional real-domain RTM. (d) Imaging result of (b) by conventional real-domain RTM.
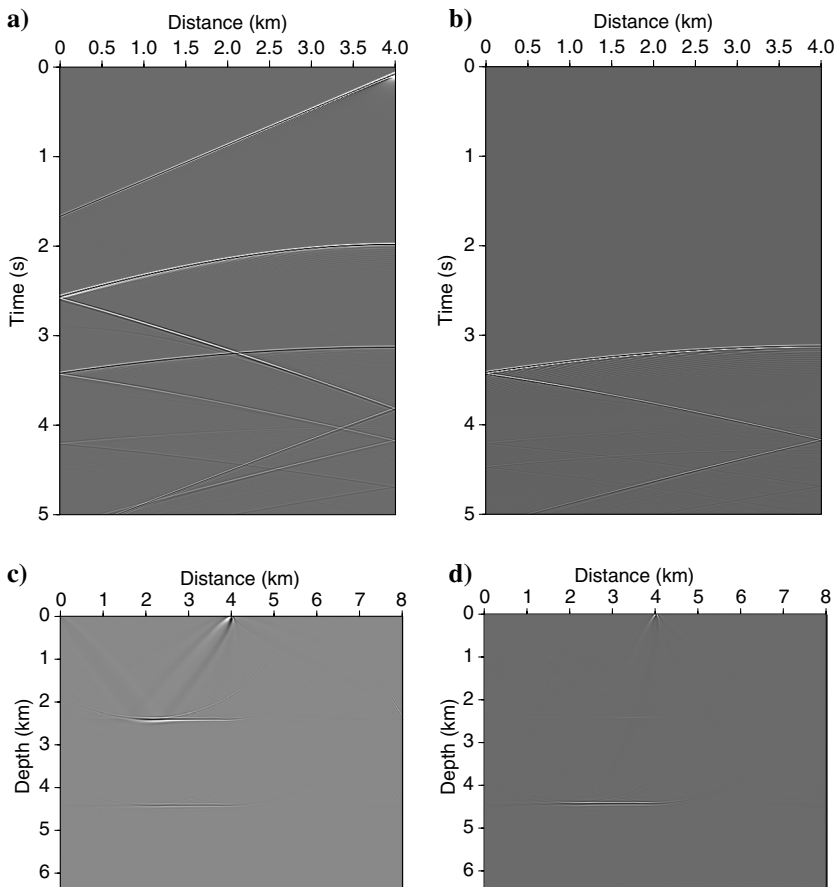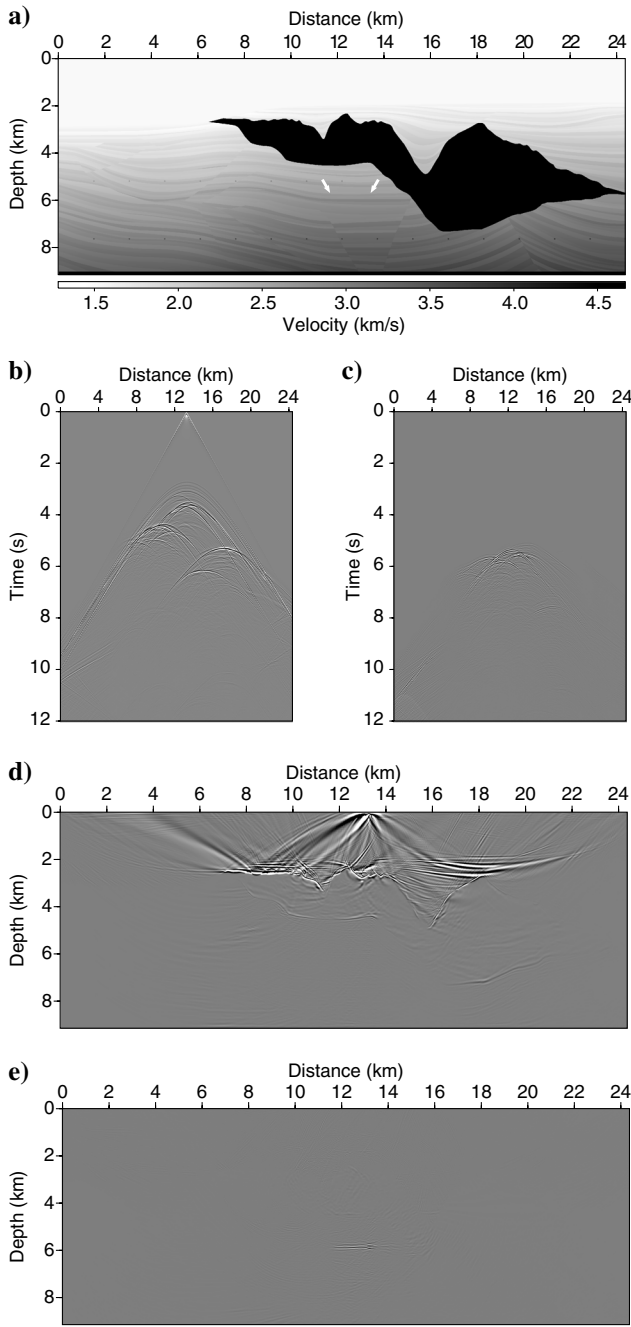
Figure 5. (a) Velocity model of Sigsbee2A; the sediment between the two arrows is the stained structure. (b) Real surface data of (a). The shot is located at 13.26 km, and the geophones are distributed from 0 to 24.39 km with an interval of 11.43 m. (c) Imaginary data corresponding to (b). (d) Imaging result of (b) by conventional real-domain RTM. (e) Imaging result of (c) by conventional real-domain RTM.

(Figure 7b), the target structures in the imaginary images (Figure 7c and 7d) are effectively highlighted, and the S/Ns of these areas are improved significantly.

Some extra costs are needed using the staining algorithm compared with conventional real-domain calculations: In the calculation of the shot wavefield, all the variables are of complex type, not the real type as in the conventional approach. In applying the imaging condition, the real and the imaginary shot wavefields are crosscorrelated with the receiver wavefield, respectively. However, there is no difference in the calculation of the receiver wavefield; therefore, we find the overall expense acceptable.

CONCLUSION

We describe a wavefield staining algorithm and apply it to seismic modeling and migration. By using this method in modeling, we can stain any target structure in the velocity model and excite an imaginary wavefield, which is synchronized with the real wavefield but only contains the response relevant to the target structure; therefore, we can trace and identify the reflections from a certain desired structure in the wavefield and the recorded data. Applying this
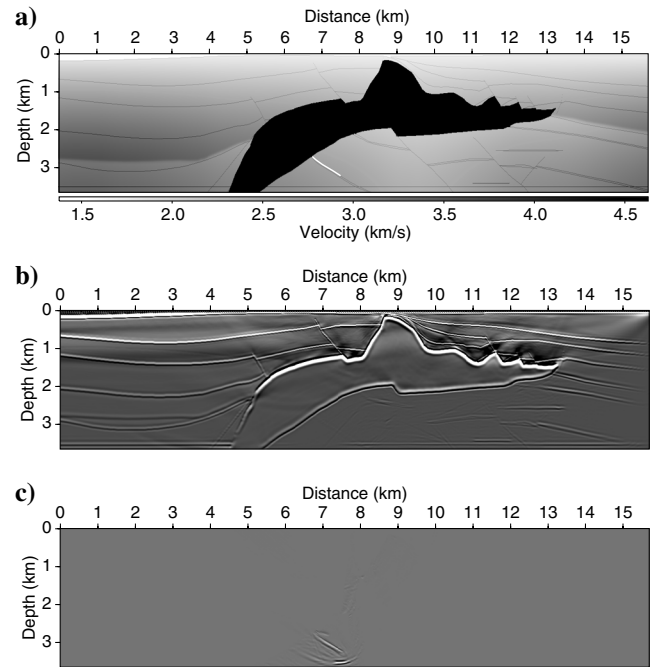

Figure 6. (a) Velocity model of the SEG/EAGE 2D profile A-A′; the white line is the stained structure. (b) Real image obtained by staining algorithm. (c) Imaginary image obtained by staining algorithm.

Table 1. The magnitude of maximal difference and $\gamma(k)$ with the variation of k.

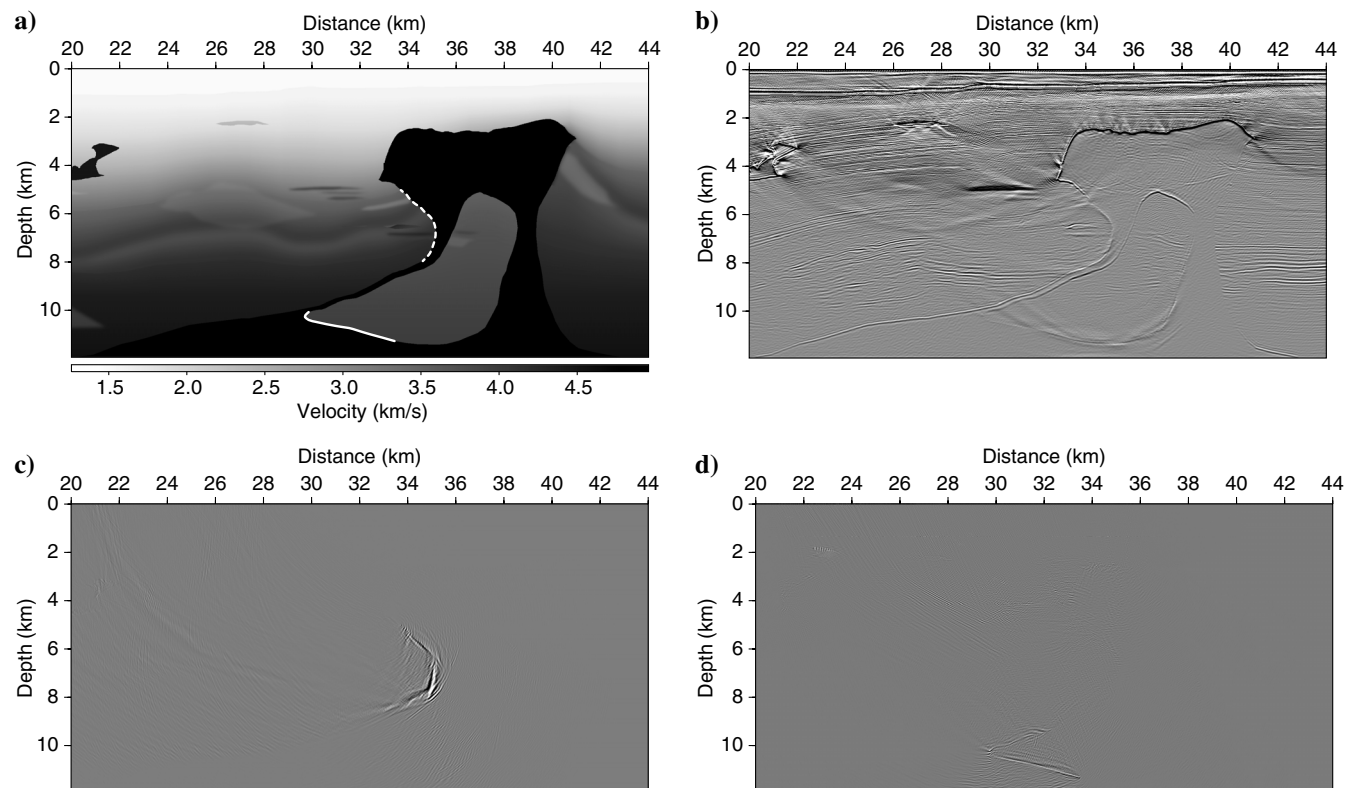| k	1	2	3	4	5	≥ 6
$\max \lvert p(x,z) - \bar{p}^{(k)}(x,z) \rvert$	1.75×10^{-6}	1.26×10^{-7}	1.05×10^{-7}	1.10×10^{-7}	8.23×10^{-8}	0.00
$\gamma(k)$	5.69×10^{-4}	4.10×10^{-5}	3.41×10^{-5}	3.57×10^{-5}	2.68×10^{-5}	0.00

Figure 7. (a) Velocity model of BP 2D benchmark data set; the white dashed line is the stained structure 1, and the white solid line is the strained structure 2. (b) Real image obtained by staining algorithm. (c) Imaginary image obtained by staining algorithm (target 1). (d) Imaginary image obtained by staining algorithm (target 2).

method to migration, we can effectively mute reflections of nontarget structures in the imaginary shot wavefield. Beside the conventional RTM image, we can simultaneously obtain an image of the target region with the S/N significantly improved. Numerical examples on various models give satisfactory modeling and imaging results. Implementation of this method is easy and independent of a specific migration operator. It can be easily used by any popular migration approach to enhance the image quality of critical structures. This method is also potential in quantitative illumination analysis and velocity model building.

ACKNOWLEDGMENTS

REFERENCES

Albertin, U., D. Watts, W. Chang, S. J. Kapoor, C. Stork, P. Kitchenside, and D. Yingst, 2002, Near-salt-flank imaging with Kirchhoff and wavefield extrapolation migration: 72nd Annual International Meeting, SEG, Expanded Abstracts, 1328–1331.
Baysal, E., D. D. Kosloff, and J. W. C. Sherwood, 1983, Reverse time migration: Geophysics, 48, 1514–1524, doi: 10.1190/1.1441434.
Burch, T., B. Hornby, H. Sugianto, and B. Nolte, 2010, Subsalt 3D VSP imaging at Deimos Field in the deepwater Gulf of Mexico: The Leading Edge, 29, 680–685, doi: 10.1190/1.3447781.
Cao, J., and R. S. Wu, 2009, Fast acquisition aperture correction in prestack depth migration using beamlet decomposition: Geophysics, 74, no. 4, S67–S74, doi: 10.1190/1.3116284.
Dale, L., and J. M. W. Slack, 1987, Fate map for the 32-cell stage of Xenopus laevis: Development, 99, 527–551.
Fliedner, M., M. Brown, D. Bevc, and B. Biondi, 2007, Wavepath tomography for subsalt velocity-model building: 77th Annual International Meeting, SEG, Expanded Abstracts, 1938–1942.
Fowler, P. J., E. Mobley, and B. Hootman, 2004, The importance of anisotropy and turning rays in prestack time migration: 74th Annual International Meeting, SEG, Expanded Abstracts, 1013–1016.
Gherasim, M., U. Albertin, B. Nolte, and O. Askim, 2010, Wave-equation angle-based illumination weighting for optimized subsalt imaging: 80th Annual International Meeting, SEG, Expanded Abstracts, 3293–3297.
Gilbert, S. F., 2000, Developmental biology, 6th ed.: Sinauer Associates.
Ginhoux, F., M. Greter, M. Leboeuf, S. Nandi, P. See, S. Gokhan, M. F. Mehler, S. J. Conway, L. G. Ng, E. R. Stanley, I. M. Samokhvalov, and M. Merad, 2010, Fate mapping analysis reveals that adult microglia derive from primitive macrophages: Science, 330, 841–845, doi: 10.1126/science.1194637.
Jackson, M. P. A., B. C. Vendeville, and D. D. Schultz-Ela, 1994, Salt-related structures in the Gulf of Mexico: A field guide for geophysicists: The Leading Edge, 13, 837–842, doi: 10.1190/1.1437040.
Ji, S., T. Huang, K. Fu, and Z. Li, 2011, Dirty salt velocity inversion: The road to a clearer subsalt image: Geophysics, 76, no. 5, WB169–WB174, doi: 10.1190/geo2010-0392.1.

Jia, X., and R. S. Wu, 2009, Superwide-angle one-way wave propagator and its application in imaging steep salt flanks: Geophysics, **74**, no. 4, S75–S83, doi: 10.1190/1.3124686.

Kapoor, J., N. Moldevaneau, M. Egan, M. O'Briain, D. Desta, I. Atakish-iyev, M. Tomida, and L. Stewart, 2007, Subsalt imaging: The RAZ-WAZ experience: The Leading Edge, **26**, 1414–1422, doi: 10.1190/1.2805764.

Leveille, J., I. Jones, Z. Zhou, B. Wang, and F. Liu, 2011, Subsalt imaging for exploration, production, and development: A review: Geophysics, **76**, no. 5, WB3–WB20, doi: 10.1190/geo2011-0156.1.

Liu, Y., X. Chang, D. Jin, R. He, H. Sun, and Y. Zheng, 2011, Reverse time migration of multiples for subsalt imaging: Geophysics, **76**, no. 5, WB209–WB216, doi: 10.1190/geo2010-0312.1.

Malcolm, A. E., B. Ursin, and M. V. de Hoop, 2008, Subsalt imaging with internal multiples: 78th Annual International Meeting, SEG, Expanded Abstracts, 2461–2465.

McMechan, G. A., 1983, Migration by extrapolation of time-dependent boundary values: Geophysical Prospecting, **31**, 413–420, doi: 10.1111/j.1365-2478.1983.tb01060.x.

Muerdter, D., and D. Ratcliff, 2001, Understanding subsalt illumination through ray-trace modeling, Part 1: Simple 2-D salt models: The Leading Edge, **20**, 578–594, doi: 10.1190/1.1438998.

Mulder, W. A., and R.-E. Plessix, 2004, A comparison between one-way and two-way wave-equation migration: Geophysics, **69**, 1491–1504, doi: 10.1190/1.1836822.

Ristow, D., and T. Ruhl, 1994, Fourier finite-difference migration: Geophysics, **59**, 1882–1893, doi: 10.1190/1.1443575.

Sava, P., and S. Fomel, 2005, Riemannian wavefield extrapolation: Geophysics, **70**, no. 3, T45–T56, doi: 10.1190/1.1925748.

Shen, H., S. Mothi, and U. Albertin, 2011, Improving subsalt imaging with illumination-based weighting of RTM 3D angle gathers: 81st Annual International Meeting, SEG, Expanded Abstracts, 3206–3211.

Sheriff, R. E., and L. P. Geldart, 1995, Exploration seismology, 2nd ed.: Cambridge University Press.

Shragge, J., and G. Shan, 2008, Prestack wave-equation depth migration in elliptical coordinates: Geophysics, **73**, no. 5, S169–S175, doi: 10.1190/1.2956349.

Symes, W. W., 2007, Reverse time migration with optimal checkpointing: Geophysics, **72**, no. 5, SM213–SM221, doi: 10.1190/1.2742686.

Tang, Y., and B. Biondi, 2011, Target-oriented wavefield tomography using synthesized Born data: Geophysics, **76**, no. 5, WB191–WB207, doi: 10.1190/geo2010-0383.1.

VerWest, B., and D. Lin, 2007, Modeling the impact of wide-azimuth acquisition on subsalt imaging: Geophysics, **72**, no. 5, SM241–SM250, doi: 10.1190/1.2736516.

Wang, B., Y. Kim, C. Mason, and X. Zeng, 2008, Advances in velocity model-building technology for subsalt imaging: Geophysics, **73**, no. 5, VE173–VE181, doi: 10.1190/1.2966096.

Yang, T. N., J. Shragge, and P. Sava, 2012, Illumination compensation for subsalt image-domain wavefield tomography: 82nd Annual International Meeting, SEG, Expanded Abstracts, doi: 10.1190/segam2012-0563.1.

Zhang, J., and G. A. McMechan, 1997, Turning wave migration by horizontal extrapolation: Geophysics, **62**, 291–297, doi: 10.1190/1.1444130.

Zhu, X., J. Cao, D. Ashabranner, S. Sood, J. Brewer, and C. Mosher, 2012, Advanced modeling and imaging for seismic acquisition — A GOM subsalt example: 82nd Annual International Meeting, SEG, Expanded Abstracts, doi: 10.1190/segam2012-0858.1.